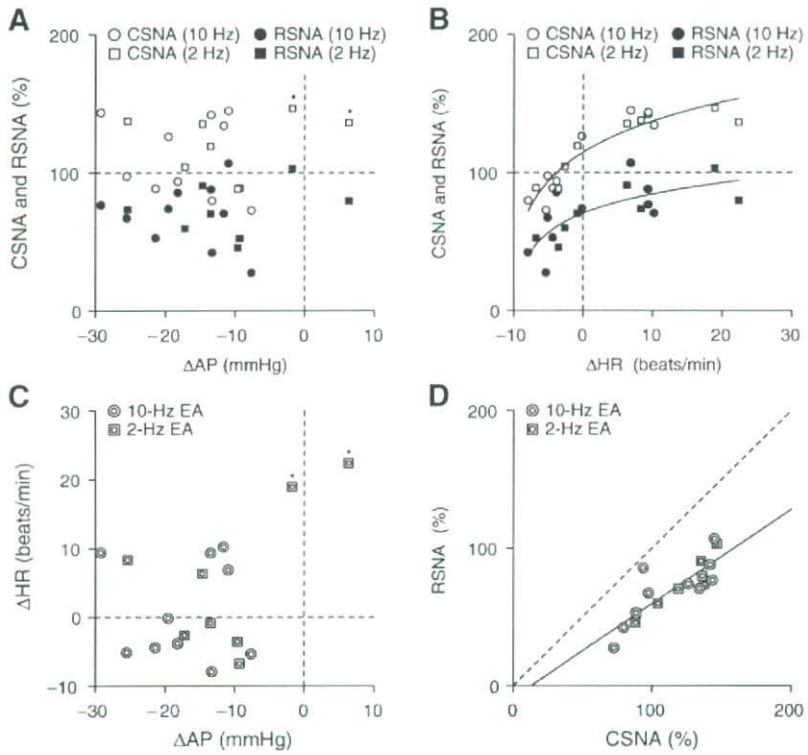

Fig. 3. Scatter plots of data obtained from the last 10 s of 1-min electroacupuncture (EA). A: Percent values of cardiac sympathetic nerve activity (CSNA) and renal sympathetic nerve activity (RSNA) plotted against changes in arterial pressure (ΔAP). Open and closed circles indicate CSNA and RSNA during 10-Hz EA, respectively. Open and closed squares indicate CSNA and RSNA during 2-Hz EA, respectively. Open squares with asterisks indicate data points where CSNA increased during EA even when AP did not decrease significantly or even increased. There was no significant relationship between changes in AP and CSNA ($r^2=0.0025$, $P=0.84$) or RSNA ($r^2=0.0039$, $P=0.81$). B: CSNA and RSNA plotted against changes in heart rate (ΔHR). Positive curvilinear relationships were observed between ΔHR and CSNA [$CSNA=83.0\times\log_{10}(11.5+\Delta HR)+26.7$, $r^2=0.86$, $P<0.01$] and between ΔHR and RSNA [$RSNA=46.6\times\log_{10}(10.1+\Delta HR)+23.6$, $r^2=0.56$, $P<0.01$]. C: Scatter plots of ΔHR versus ΔAP during 10-Hz EA (double circles) and 2-Hz EA (double squares). Except for the two data points with asterisks, there was no apparent relationship between changes in AP and those in HR ($r^2=0.17$, $P=0.094$ when the points with asterisk were included; $r^2=0.048$, $P=0.41$ when the points with asterisk were excluded). D: Scatter plots of RSNA versus CSNA during 10-Hz EA (double circles) and 2-Hz EA (double squares). There was a quasi-linear relationship between RSNA and CSNA ($RSNA=0.69\times CSNA-8.8$, $r^2=0.71$, $P<0.01$). The dashed line indicates the line of identity.

the cessation of EA. HR was significantly decreased in the first 20 s of EA but returned to the baseline level thereafter while EA continued. There was large variance in the CSNA response to EA among animals. Only the increase in CSNA after the cessation of EA was statistically significant. In contrast, RSNA was significantly decreased by EA during the entire period of EA.

Fig. 2B summarizes changes in AP, HR, CSNA, and RSNA in response to 2-Hz EA. We pooled data for 8 trials from 4 animals (left and right trials in each animal). Baseline AP and HR values were 98 ± 17 mmHg and 151 ± 20 beats/min, respectively. AP was decreased by EA, but the decrease was smaller and the duration of post-EA hypotension shorter than those observed in 10-Hz EA. HR increased with large variance during EA, and the increase was statistically significant after the cessation of EA. CSNA increased during the last 30 s of EA and remained increased for approximately 10 s after the cessation of EA. RSNA was decreased by EA during the period of EA, but the decrease appeared to be smaller than that observed with 10-Hz EA.

Fig. 3 illustrates scatter plots of data obtained during the last 10 s of EA. Because changes in AP nearly reached the steady state during the last 10 s of EA (Fig. 2A and B), we focused on these data. Open and closed circles in Fig. 3A and B indicates CSNA and RSNA data obtained from 10-Hz EA, respectively. Open and closed squares indicate CSNA and RSNA data obtained from 2-Hz EA, respectively. There was no apparent relationship between changes in AP and CSNA ($r^2=0.0025$, $P=0.84$) or RSNA ($r^2=0.0039$, $P=0.81$) by a linear regression analysis (Fig. 3A). In contrast, a positive curvilinear relationship was observed between changes in HR and CSNA [$CSNA=83.0\times\log_{10}(11.5+\Delta HR)+26.7$, $r^2=0.86$, $P<0.01$] or RSNA [$RSNA=46.6\times\log_{10}(10.1+\Delta HR)+23.6$, $r^2=0.56$, $P<0.01$] (Fig. 3B). Double circles and squares in Fig. 3C and D indicate data obtained from 10-Hz EA and 2-Hz EA, respectively. In Fig. 3C, the two data points with asterisks indicate that 2-Hz EA increased HR by approximately 20 beats/min when changes in AP were close to zero or positive. However, except for the two data points, there was no apparent relationship between changes in AP and changes in HR ($r^2=0.17$, $P=0.094$ when the points with asterisk were included; $r^2=0.048$, $P=0.41$ when the points with asterisk were excluded). As indicated by Fig. 3A and B, the RSNA values were lower than the corresponding CSNA data (Fig. 3D), though CSNA and RSNA were both normalized to 100% during the baseline condition. A linear regression analysis revealed a significant positive correlation between CSNA and RSNA during the last 10 s of EA ($RSNA=0.69\times CSNA-8.8$, $r^2=0.71$, $P<0.01$).

As shown in Fig. 4A, there were no significant changes in AP, HR, CSNA, or RSNA during stimulation applied to a control point in the front of the right thigh. Baseline AP and HR values were 92 ± 15 mmHg and 158 ± 16 beats/min, respectively.

After sinoaortic denervation and vagotomy, baseline AP and HR values were 120 ± 25 mmHg and 184 ± 19 beats/min, respectively. As shown in Fig. 4B, 10-Hz EA decreased AP by approximately 30 mmHg. AP returned gradually to the pre-EA value after the cessation of EA. HR decreased slightly from 20 to 30 s and returned to the pre-EA baseline value thereafter. CSNA decreased only at the onset of EA. After the cessation of EA, CSNA exhibited a slight increase for approximately 20 s. RSNA decreased at the onset of EA. Although the magnitude of RSNA decrease became smaller with time, RSNA remained decreased during the period of EA.

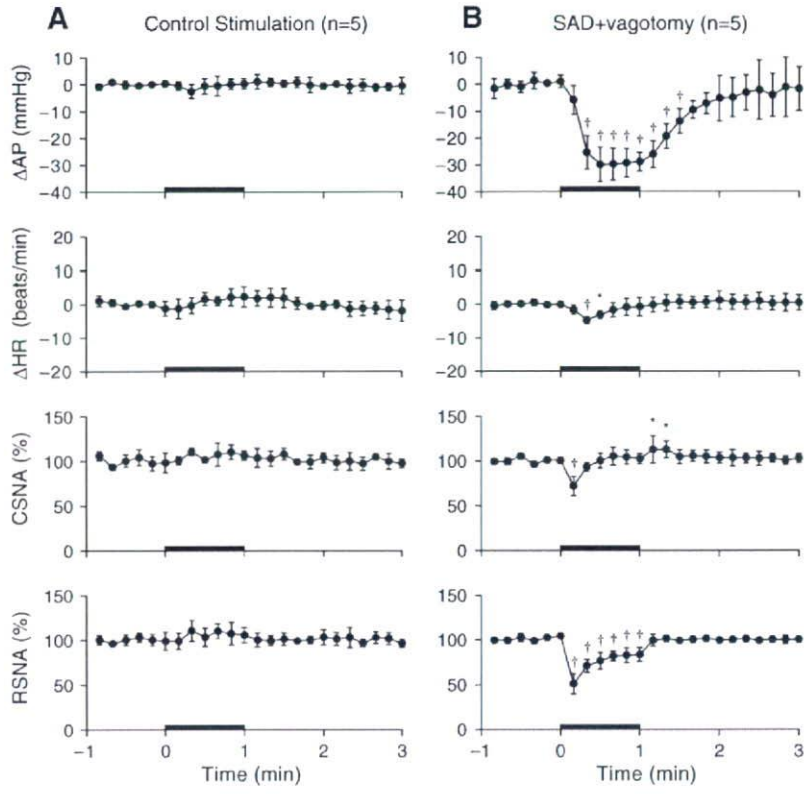

Fig. 4. Changes in arterial pressure (ΔAP), changes in heart rate (ΔHR), percent values of cardiac sympathetic nerve activity (CSNA), and percent values of renal sympathetic nerve activity (RSNA) during electrical stimulation at a nonspecific control point (A) and 10-Hz electroacupuncture (EA) after sinoaortic denervation (SAD) and vagotomy (B) averaged for all trials. Values are the mean±SD. *$P<0.05$ and †$P<0.01$ from the first data point during pre-EA baseline period.

Fig. 5A depicts changes in AP, HR, CSNA, and RSNA induced by intravenous bolus injection of phenylephrine (5 μg/kg). The data were obtained before sinoaortic denervation and vagotomy. Baseline AP and HR values were 98±24 mmHg and 163±30 beats/min, respectively. As expected, phenylephrine increased AP but decreased HR. Both CSNA and RSNA were decreased by phenylephrine injection. The suppression of CSNA persisted longer than that of RSNA. There was no significant correlation between CSNA and RSNA during the baseline condition immediately before the administration of phenylephrine (Fig. 5B, white circles, $r^2=0.32$, $P=0.32$). When CSNA and RSNA were compared during the time period of phenylephrine-induced maximum AP elevation, there was no significant correlation either (Fig. 5B, filled circles, $r^2=0.0003$, $P=0.98$).

4. Discussion

We have demonstrated that CSNA and RSNA responded differentially to EA applied to a hind limb in pentobarbital-anesthetized cats. Although the CSNA and RSNA responses were discordant, we found that CSNA and RSNA attained a new linear relationship during the last 10 s of EA (Fig. 3D), regardless of the stimulus frequency of EA.

4.1. Effects of EA on CSNA and RSNA

The neural mechanisms underlying hemodynamic responses to acupuncture are not fully understood. Recently, Uchida et al. (2007) demonstrated that manual acupuncture-like stimulation of a hind limb decreased CSNA and HR in pentobarbital-anesthetized rats. Their results complement the study by Ohsawa et al. (1995) showing that manual acupuncture-like stimulation decreased RSNA and AP. Although these results suggest that manual acupuncture-like stimulation causes systemic sympathoinhibition, we noted that HR did not necessarily decrease even when EA produced hypotensive effects in pentobarbital-anesthetized cats (Figs. 1A and 2A and B). Simultaneous recordings of CSNA and RSNA in the present study clearly supported the hypothesis that EA evoked regional differences among sympathetic nerve activities. Fig. 1A is a typical case in which CSNA increased without an associated increase in RSNA during the later portion of EA. In Protocol 2, no significant changes were observed (Fig. 4A), suggesting that hemodynamic and sympathetic nerve activity responses observed in Protocol 1 were not nonspecific responses to electrical stimulation. This does not mean, however, the point below the knee joint just lateral to the tibia (corresponding to an ST36 acupoint in humans) is the only specific point to produce cardiovascular responses. For instance, EA at the forelimb (corresponding to a PC6 acupoint in humans) exerts the cardiovascular effects in rats (Lujan et al., 2007).

Averaged data for 10-Hz EA (Fig. 2A) revealed a discrepancy between the CSNA and RSNA responses to EA. Both sympathoinhibition and sympathoexcitation appear to have occurred in CSNA during EA. We suspected that strong electrical stimulation might have caused nociceptive sympathoexcitatory responses in CSNA. However, reducing the stimulus frequency from 10 to 2 Hz resulted in a more pronounced excitatory response in CSNA during the later period of 1-min EA (Fig. 2B), suggesting that the increase in CSNA during EA was not a nociceptive response. Another factor that should be taken into account is effects of anesthesia. Matsukawa et al. (Matsukawa et al., 1993) demonstrated that sympathoinhibition induced by acute intravenous pentobarbital administration was larger and lasted longer in the case of CSNA than in that of RSNA in cats. The sympathoinhibitory response to EA may be easily observed when the baseline sympathetic tone is high. Because baseline sympathetic tone was probably lower in CSNA than in RSNA due to the pentobarbital anesthesia, the sympathoinhibitory response in CSNA might have been masked or hard to observe.

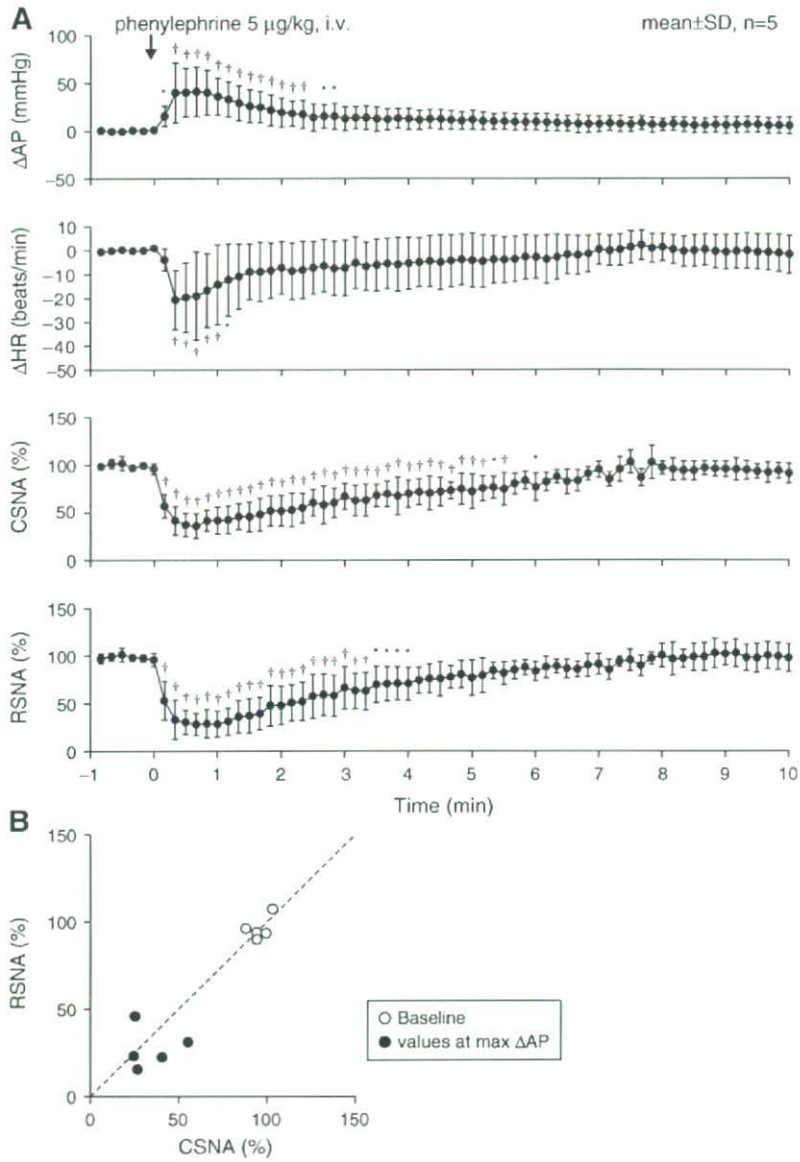

Fig. 5. A: Changes in arterial pressure (ΔAP), changes in heart rate (ΔHR), percent values of cardiac sympathetic nerve activity (CSNA), and percent values of renal sympathetic nerve activity (RSNA) during intravenous bolus injection of phenylephrine (5 μg/kg). Values are the mean ± SD. *$P<0.05$ and †$P<0.01$ from the first data point during the baseline period. B: Scatter plots between CSNA and RSNA during the baseline condition immediately before the administration of phenylephrine (white circles) and those during the time period of phenylephrine-induced maximum AP elevation (filled circles). There was no significant correlation between CSNA and RSNA. The dashed line indicates the line of identity.

Although we measured left CSNA near the ventral ansa of the left stellate ganglion, there are several connections between the vagal and sympathetic nerves to form the cardiopulmonary nerves (Armour and Hopkins, 1984). Because we did not cut the vagi at the neck in Protocols 1 and 2, possibility of vagal contamination in the CSNA recording cannot be ruled out. However, because phenylephrine-induced hypertension that can increase vagal efferent activity (Kawada et al., 2001) attenuated CSNA to a similar degree to RSNA during the time period of maximum AP elevation (38.5 ± 13.4% vs. 28.6 ± 10.5%, $P=0.32$ by paired-t test, Fig. 5A), the effect of vagal contamination might have been a limited one.

4.2. Mechanistic considerations

In the present experimental settings, CSNA and RSNA exhibited decreasing responses to arterial baroreflex activation as demonstrated in previous studies (Fig. 5) (Minisi et al., 1989; Ninomiya et al., 1971), confirming that what we measured as CSNA and RSNA represented efferent sympathetic nerve activities. Because EA caused hypotension, it could exert sympathoexcitatory effects through the arterial baroreflex in Protocol 1. If the baroreflex-mediated sympathoexcitatory effect is stronger for CSNA than for RSNA, this may account for the discrepancy between the CSNA and RSNA responses. However, in some trials, CSNA was increased even when AP did not decrease sizably or was even increased (Fig. 3A, open squares with asterisks), suggesting that the baroreflex-medicated sympathoexcitatory effect cannot explain the increase in CSNA. Actually, the discrepancy between the CSNA and RSNA responses to 10-Hz EA persisted after sinoaortic denervation and vagotomy (Fig. 4B). Therefore, CSNA might have been activated in the later period of EA via mechanisms other than baroreflexes. This interpretation is in line with the conclusion by Sato et al. (1981) that variable changes in HR in response to somatic afferent stimulation were not an indirect consequence of preceding changes in blood pressure.

Although electrical stimulation of groups I and II muscle nerves of fore and hind limbs was not effective in changing HR (McCloskey and Mitchell, 1972; Sato et al., 1981), additional stimulation of group III nerves induced either tachycardia or bradycardia in anesthetized cats (Khayutin et al., 1986; Sato et al., 1981). Further, additional stimulation of group IV muscle nerves of a hind limb always produced tachycardia (Johansson, 1962; Tibes, 1977), with an optimal frequency between 6 and 15 Hz (Sato et al., 1981). In the present study, activation of group IV muscle nerves unlikely explain the tachycardiac response, since reducing the stimulus frequency from 10 to 2 Hz did not attenuate the tachycardiac response. Although Sato et al. (1981) concluded that whether group III muscle afferent stimulation induces tachycardia or bradycardia was difficult to predict, we found that there was a quasi-linear relationship between RSNA and CSNA during the last 10 s of 1-min EA, regardless of the stimulus frequency (Fig. 3D). When the sympathoinhibition assessed by RSNA was strong enough, CSNA decreased during EA. When the sympathoinhibition assessed by RSNA was weak, CSNA increased.

4.3. Limitations

Several limitations need to be addressed. First, we performed experiments under pentobarbital anesthesia. Our results might have differed had we used different anesthesia or performed the experiments in conscious animals. However, Sato et al. (1981) used chloralose and urethane anesthesia and reported divergence of HR responses induced by group III muscle fiber afferent stimulation. Therefore, the differences between CSNA and RSNA might not be explained by type of anesthesia alone.

Second, we measured only CSNA and RSNA. Changes in AP did not correlate with CSNA or RSNA (Fig. 3A), suggesting that the AP response to EA was not explained by changes in CSNA or RSNA. The abdominal vascular bed plays a significant role in the arterial blood pressure control (Rowell, 1974). Further studies such as that recording splanchnic nerve activity are needed to elucidate the total picture of the sympathetic mechanism for the AP response to EA.

Third, we did not perform vagotomy independently of sinoaortic denervation. Accordingly, the contribution of vagal nerve activity to the HR response was not identified. Comparing Figs. 2A and 4B, the initial drop in HR was much clearer before sinoaortic denervation and vagotomy ($P = 0.025$ during the first 10 s after EA initiation by unpaired-t test) despite the similar profile of CSNA response to EA. Therefore, the vagal nerve activity might have contributed to the initial drop in HR in response to EA.

4.4. Conclusion

We demonstrated that EA evoked regional differences between CSNA and RSNA in pentobarbital-anesthetized cats. The differences persisted after sinoaortic denervation and vagotomy, suggesting the baroreflex-mediated sympathoexcitatory mechanisms alone cannot explain the discrepancy between CSNA and RSNA responses during EA. Although the responses were discordant, there was a linear relationship that persisted between CSNA and RSNA during the last 10 s of 1-min EA, suggesting that EA changes the relationship between CSNA and RSNA.

Acknowledgments

This study was supported by a "Health and Labour Sciences Research Grant for Research on Advanced Medical Technology", "Health and Labour Sciences Research Grant for Research on Medical Devices for Analyzing, Supporting, and Substituting the Function of the Human Body", and a "Health and Labour Sciences Research Grant (H18-Iryo-Ippan-023) (H18-Nano-Ippan-003)", from the Ministry of Health, Labour, and Welfare of Japan, the "Industrial Technology Research Grant Program" of the New Energy and Industrial Technology Development Organization of Japan.

References

Armour, J.A., Hopkins, D.A., 1984. Anatomy of the extrinsic efferent autonomic nerves and ganglia innervating the mammalian heart. In: Randall, W.C. (Ed.), Nervous Control of Cardiovascular Function. Oxford Univ. Press, New York, pp. 20–45.

DiBona, G.F., 2005. Physiology in perspective: the wisdom of the body. Neural control of the kidney. Am. J. Physiol., Regul. Integr. Comp. Physiol. 289 (3), R633–641.

Glantz, S.A., 2002. Primer of Biostatistics, 5th ed. McGraw-Hill, New York.

Johansson, B., 1962. Circulatory responses to stimulation of somatic afferents with special reference to depressor effects from muscle nerves. Acta Physiol. Scand., Suppl. 198, 1–91.

Kawada, T., Yamazaki, T., Akiyama, T., Shishido, T., Inagaki, M., Uemura, K., Miyamoto, T., Sugimachi, M., Takaki, H., Sunagawa, K., 2001. In vivo assessment of acetylcholine-releasing function at cardiac vagal nerve terminals. Am. J. Physiol. Heart Circ. Physiol. 281 (1), H139–145.

Kawada, T., Uemura, K., Kashihara, K., Jin, Y., Li, M., Zheng, C., Sugimachi, M., Sunagawa, K., 2003. Uniformity in dynamic baroreflex regulation of left and right cardiac sympathetic nerve activities. Am. J. Physiol., Regul. Integr. Comp. Physiol. 284 (6), R1506–1512.

Khayutin, V.M., Lukoshkova, E.V., Gailans, J.B., 1986. Somatic depressor reflexes: results of specific 'depressor' afferents' excitation or an epiphenomenon of general anesthesia and certain decerebrations? J. Auton. Nerv. Syst. 16 (1), 35–60.

Kimura, A., Sato, A., 1997. Somatic regulation of autonomic functions in anesthetized animals—neural mechanisms of physical therapy including acupuncture. Jpn. J. Vet. Res. 45 (3), 137–145.

Kline, R.L., Yeung, K.Y., Calaresu, F.R., 1978. Role of somatic nerves in the cardiovascular responses to stimulation of an acupuncture point in anesthetized rabbits. Exp. Neurol. 61 (3), 561–570.

Kobayashi, S., Noguchi, E., Ohsawa, H., Sato, Y., Nishijo, K., 1998. Experimental research on the reflex decrease of heart rate elicited by acupuncture stimulation in anesthetized rats (in Japanese). Jpn. Acupunct. Moxib. 48, 120–129.

Ku, Y.H., Zou, C.J., 1993. Tinggong (SI 19), a novel acupoint for 2 Hz electroacupuncture-induced depressor response. Acupunct. Electrother. Res. 18 (2), 89–96.

Lee, H.S., Kim, J.Y., 1994. Effects of acupuncture on blood pressure and plasma renin activity in two-kidney one clip Goldblatt hypertensive rats. Am. J. Chin. Med. 22 (3–4), 215–219.

Lin, M.C., Nahin, R., Gershwin, M.E., Longhurst, J.C., Wu, K.K., 2001. State of complementary and alternative medicine in cardiovascular, lung, and blood research: executive summary of a workshop. Circulation 103 (16), 2038–2041.

Lujan, H.L., Kramer, V.J., DiCarlo, S.E., 2007. Electroacupuncture decreases the susceptibility to ventricular tachycardia in conscious rats by reducing cardiac metabolic demand. Am. J. Physiol. Heart Circ. Physiol. 292 (5), H2550–H2555.

Matsukawa, K., Ninomiya, I., Nishiura, N., 1993. Effects of anesthesia on cardiac and renal sympathetic nerve activities and plasma catecholamines. Am. J. Physiol. 265 (4 Pt 2), R792–R797.

McCloskey, D.I., Mitchell, J.H., 1972. Reflex cardiovascular and respiratory responses originating in exercising muscle. J. Physiol. 224 (1), 173–186.

Minisi, A.J., Dibner-Dunlap, M., Thames, M.D., 1989. Vagal cardiopulmonary baroreflex activation during phenylephrine infusion. Am. J. Physiol. 257 (5 Pt 2), R1147–R1153.

Nelder, J.A., Mead, R., 1965. A simplex method for function minimization. Comput. J. 7, 308–313.

Ninomiya, I., Nisimaru, N., Irisawa, H., 1971. Sympathetic nerve activity to the spleen, kidney, and heart in response to baroceptor input. Am. J. Physiol. 221 (5), 1346–1351.

Ohsawa, H., Okada, K., Nishijo, K., Sato, Y., 1995. Neural mechanism of depressor responses of arterial pressure elicited by acupuncture-like stimulation to a hindlimb in anesthetized rats. J. Auton. Nerv. Syst. 51 (1), 27–35.

Rowell, L.B., 1974. Human cardiovascular adjustments to exercise and thermal stress. Physiol. Rev. 54 (1), 75–159.

Sato, A., Sato, Y., Schmidt, R.F., 1981. Heart rate changes reflecting modifications of efferent cardiac sympathetic outflow by cutaneous and muscle afferent volleys. J. Auton. Nerv. Syst. 4 (3), 231–247.

Sato, A., Sato, Y., Suzuki, A., Uchida, S., 1994. Reflex modulation of gastric and vesical function by acupuncture-like stimulation in anesthetized rats. Biomed. Res. 15, 59–65.

Sato, A., Sato, Y., Uchida, S., 2002. Reflex modulation of visceral functions by acupuncture-like stimulation in anesthetized rats. Int. Congr. Ser. 1238, 111–123.

Tibes, U., 1977. Reflex inputs to the cardiovascular and respiratory centers from dynamically working canine muscles. Some evidence for involvement of group III or IV nerve fibers. Circ. Res. 41 (3), 332–341.

Uchida, S., Shimura, M., Ohsawa, H., Suzuki, A., 2007. Neural mechanism of bradycardiac responses elicited by acupuncture-like stimulation to a hind limb in anesthetized rats. J. Physiol. Sci. 57 (6), 377–382.

Yasunaga, K., Nosaka, S., 1979. Cardiac sympathetic nerves in rats: anatomical and functional features. Jpn. J. Physiol. 29 (6), 691–705.

Zhou, W., Fu, L.W., Tjen, A.L.S.C., Li, P., Longhurst, J.C., 2005. Afferent mechanisms underlying stimulation modality-related modulation of acupuncture-related cardiovascular responses. J. Appl. Physiol. 98 (3), 872–880.

SIAM J. SCI. COMPUT.
Vol. 30, No. 6, pp. 2855–2881

A PARALLEL MULTILEVEL TECHNIQUE FOR SOLVING THE BIDOMAIN EQUATION ON A HUMAN HEART WITH PURKINJE FIBERS AND A TORSO MODEL*

TAKUMI WASHIO†, JUN-ICHI OKADA†, AND TOSHIAKI HISADA‡

Abstract. In this paper, we present a multigrid method and its implementation on parallel computers to solve the bidomain equation that appears in excitation propagation analysis of the human heart with the torso. The bidomain equation is discretized with the finite element method on a composite mesh composed of a fine voxel mesh around the heart and a coarse voxel mesh covering the torso. The extracellular potential problem on the torso is formulated as a variational problem with a constraint at the interface of the fine and coarse meshes. We show that this formulation naturally satisfies the conservation property of the electric currents and fits into the multilevel adaptive solution technique framework. We also present our special treatment of the Purkinje fiber network in the multigrid algorithm where it is modeled as multiway branching lines connected to the nodes in the voxel mesh of the heart. A parallel implementation of the proposed multigrid algorithm on distributed memory computers is presented and the performance is evaluated using real-life applications.

Key words. bidomain equation, excitation propagation, torso, multigrid, composite mesh

AMS subject classifications. 65N50, 65N30, 92C30

DOI. 10.1137/070689711

1. Introduction.

The bidomain equation is a widely accepted mathematical model for describing the excitation propagation and external stimulation of heart tissue [16, 21]. It consists of two partial differential equations (PDEs) coupled to ordinary differential equations (ODEs). The two PDEs describe the intra- and extracellular electrical circuits, respectively, that are separated by cell membranes. The ODEs incorporate the behavior of the cell membranes (capacitance of the membrane and the switching of several kinds of ion channels) to determine the currents between the two circuits. As depicted in Figure 1.1, let Ω_H be the domain of the heart muscle and Γ_H the boundary of Ω_H. The explanations for the subdomains Ω_C and Ω_P outside Ω_H are given later in this section. The bidomain equation for the intracellular potential ϕ_i and the extracellular potential ϕ_e coupled through the transmembrane potential $V_\mathrm{m} = \phi_\mathrm{i} - \phi_\mathrm{e}$ on the heart muscle is given by

$$-\nabla \cdot \boldsymbol{\sigma}_\mathrm{i} \nabla \phi_\mathrm{i} = -\beta I_\mathrm{m} \text{ on } \Omega_H, \tag{1.1}$$

$$\vec{n}_H \cdot \boldsymbol{\sigma}_\mathrm{i} \nabla \phi_\mathrm{i} = 0 \text{ on } \Gamma_H, \tag{1.2}$$

$$-\nabla \cdot \boldsymbol{\sigma}_\mathrm{e} \nabla \phi_\mathrm{e} = \beta I_\mathrm{m} \text{ on } \Omega_H, \tag{1.3}$$

$$\vec{n}_H \cdot \boldsymbol{\sigma}_\mathrm{e} \nabla \phi_\mathrm{e} = J_H \text{ on } \Gamma_H, \tag{1.4}$$

$$I_\mathrm{m} = C_\mathrm{m} \frac{\partial V_\mathrm{m}}{\partial t} + I_\mathrm{ion}(V_\mathrm{m}, \boldsymbol{S}) \text{ on } \Omega_H. \tag{1.5}$$

*Received by the editors April 27, 2007; accepted for publication (in revised form) January 16, 2008; published electronically October 13, 2008. This work was supported by Core Research for Evolutional Science and Technology, Japan Science and Technology Agency.
http://www.siam.org/journals/sisc/30-6/68971.html

†Japan Science and Technology Agency CREST, Graduate School of Frontier Sciences, University of Tokyo, 5-1-5 Kashiwanoha, Kashiwa, Chiba, 277-0882, Japan (washio@sml.k.u-tokyo.ac.jp, okada@sml.k.u-tokyo.ac.jp).

‡Graduate School of Frontier Sciences, University of Tokyo, 7-3-1 Hongo, Bunkyo-ku, Tokyo, 113-0033, Japan (hisada@mech.t.u-tokyo.ac.jp).

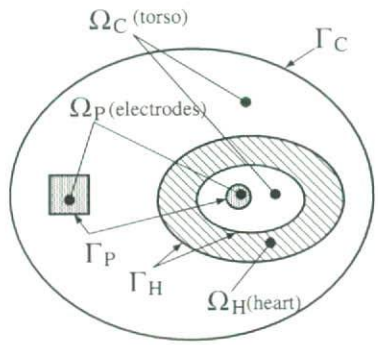

FIG. 1.1. *Two-dimensional image of the heart domain Ω_H, the torso outside the heart Ω_C, the electrodes Ω_P, and their boundaries.*

Here, $\boldsymbol{\sigma}_\mathrm{i}$ and $\boldsymbol{\sigma}_\mathrm{e}$ are the intra- and extracellular conductivity tensors, respectively, β is the surface-to-volume ratio of the tissue, C_m is the membrane capacitance per unit area, and I_m is the transmembrane current per unit area. The transmembrane current I_m is a combination of a capacitive current $C_\mathrm{m}\partial V_\mathrm{m}/\partial t$ and an ionic current $I_\mathrm{ion}(V_\mathrm{m}, \boldsymbol{S})$ passing through several kinds of ion channels, where $\boldsymbol{S}$ is a state vector composed of gating variables. The gating variables are obtained by solving the ODEs. In our simulator, the Luo–Rudy model [11] or Noble model [19] has been implemented for ventricular myocytes, while the Nattel model [5] is used for atrial myocytes. J_H is a current entering the extracellular domain of the heart through Γ_H, and $\vec{n}_H$ is the outward normal vector on Γ_H.

The intra- and extracellular conductivity tensors of the myocardium (heart muscle) are anisotropic. They are given by

$$\boldsymbol{\sigma} = c_f \boldsymbol{n}_f \otimes \boldsymbol{n}_f + c_s \boldsymbol{n}_s \otimes \boldsymbol{n}_s + c_n \boldsymbol{n}_n \otimes \boldsymbol{n}_n, \tag{1.6}$$

where $\boldsymbol{\sigma} = \boldsymbol{\sigma}_\mathrm{i}$ or $\boldsymbol{\sigma}_\mathrm{e}$. Here, $\boldsymbol{n}_f, \boldsymbol{n}_s$, and $\boldsymbol{n}_n$ denote the fiber, sheet, and sheet-normal directions, respectively, in the orthonormal basis [8]. The bases vary depending on the position in the heart. In general, the conductivity along the fiber direction c_f is the largest of the three. The orientations of the myocytes (fiber directions) have been modeled based on anatomical observations. Figure 1.2 depicts the distributions of the fiber directions in our simulation. The muscle fibers have a helical structure within the left ventricle (LV). Based on histological studies, fiber directions can be determined as the orientation of a fiber varies from $+90°$ to $-60°$ relative to the circumferential direction in a plane perpendicular to the transmural direction from the endocardiac to the epicardiac layer, resulting in a very realistic model for the fiber directions. Table 1.1 gives the conductivities in the three directions and the surface-to-volume ratio for our simulations. These conductivities are at least two times larger than the standard values. Due to the limitation of our computational resources, the local mesh size is set to 0.4 mm, which is still too large to obtain a proper wave propagation velocity (less than 0.1 mm is required). The conductivities have therefore been adjusted in order to obtain a usable wave propagation velocity.

Strong demands from physiological application areas require three-dimensional simulations to include the torso surrounding the heart as well. Physically, cardiac electrical activity results in a current flow in the torso via the extracellular potential

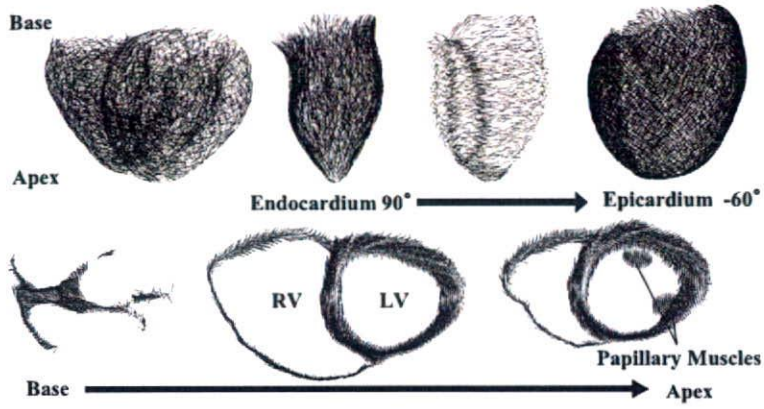

FIG. 1.2. *Fiber directions in the ventricles. The orientation of a fiber varies from* $+90^\circ$ *to* -60° *relative to the circumferential direction in a plane perpendicular to the transmural direction from the endocardiac to the epicardiac layer.*

TABLE 1.1
Conductivities [mS/cm] of the myocardial cells and the surface-to-volume ratio of the tissue β *[1/cm].*

Cells	Intra (f, s, n)	Extra (f, s, n)	β
Ventricle	7.2, 2.4, 2.0	6.0, 3.0, 3.0	2000
Atrium	7.0, 7.0, 7.0	7.0, 7.0, 7.0	2000

field. Thus, the extracellular PDE should be extended from the heart to the torso via the boundary current J_H in (1.4).

One of the applications that requires the torso model is the simulation of an implantable cardioverter defibrillator (ICD) [10]. This device delivers a strong electrical shock to the heart through the electrodes when a fatal arrhythmia is detected, as depicted in Figure 1.3. By optimizing the arrangement of electrodes and the temporal profile of the electrical current, an ICD can be developed that is much more comfortable than the device currently used.

The other important application is a simulation of the electrocardiogram (ECG) routinely used in clinical practice. In order to reproduce the ECG based on the real physiological system, modeling of the so-called Purkinje fiber network is indispensable. The Purkinje fibers are located on the inner ventricular walls of the heart with large free-running sections. They are some of the specialized cardiac muscle fibers that form the impulse-conducting network of the heart. They transmit impulses rapidly from the atrioventricular node to the ventricles. In our simulator, the DiFrancesco–Noble cell model [6] is used for the Purkinje fibers and the network has been modeled from the atrioventricular node to the myocardium. With this model, we can analyze the relations between the body surface potential and the excitation propagation in the heart in a healthy condition and in various conditions involving heart disease. This research, therefore, contributes to the early recognition and treatment through diagnosis with an ECG. Furthermore, a mechanism of arrhythmia that originates from the Purkinje fiber network, and the impact of the Purkinje fiber network at defibrillation, will be clarified by these simulations. Figure 1.4 shows the first half of one normal heart beat as computed by our simulator. In the upper part, the membrane potentials

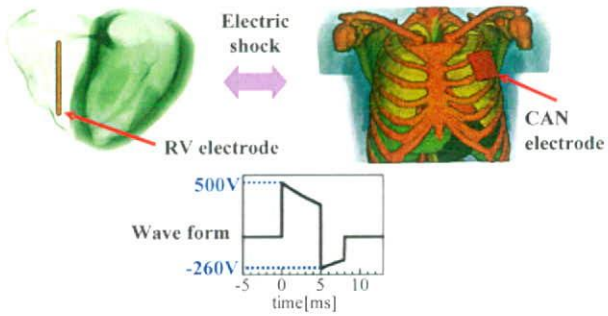

FIG. 1.3. *Two electrodes of an ICD and a typical voltage profile between them.*

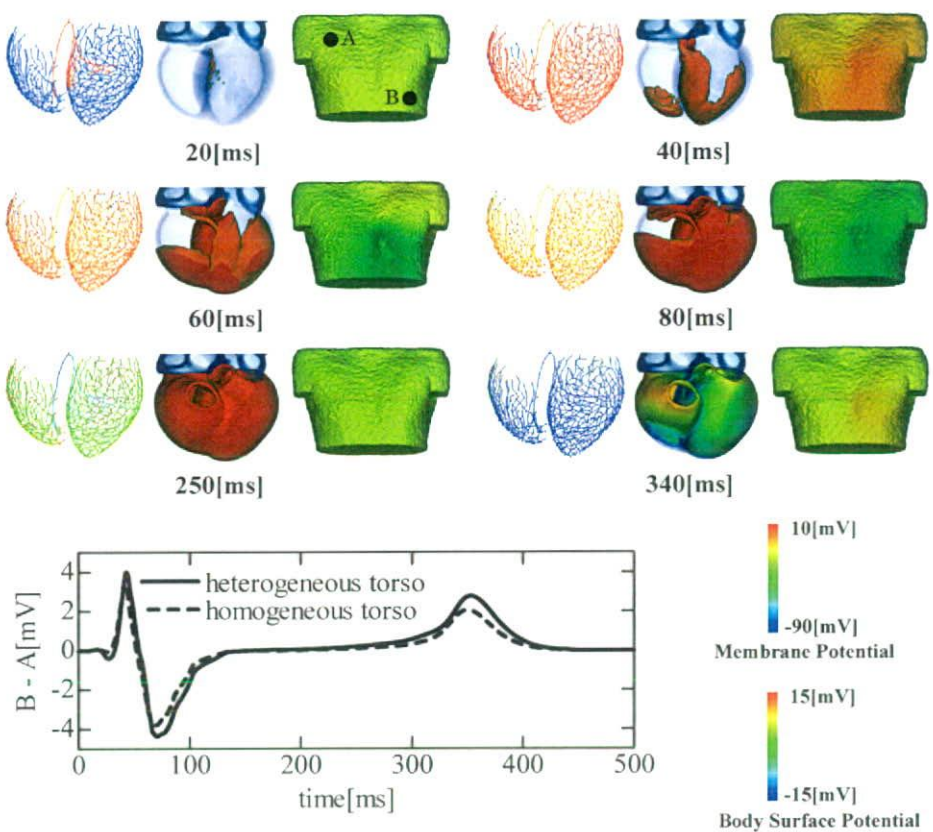

FIG. 1.4. *Membrane potentials on the Purkinje fiber network and on the heart muscle, and the surface potential on the torso at typical times. At the bottom, the second-lead ECG (difference of the potential values between points A and B) is presented for cases with the heterogeneous (rigid line) and homogeneous (broken line) torso model.*

on the Purkinje fiber and on the heart muscle, and the body surface potentials are depicted at typical times. At the bottom of the figure, the second-lead ECG obtained from this computation is depicted. This agrees well with actual clinical observations.

The mathematical formulation for the extension of the extracellular potential equation to the torso is given as follows. As depicted in Figure 1.1, let Ω_C be the torso domain outside the heart, Γ_C its boundaries, $\boldsymbol{\sigma}_c$ the electric conductivity tensor, and ϕ_c the potential on Ω_C. We assume that there are some regions inside Ω_C where electrodes with given potentials ϕ_p are imbedded in the case of an ICD simulation. We represent these electrode regions by Ω_P. In this situation, the following equations are further imposed on Ω_C in addition to (1.1)–(1.4):

$$-\nabla \cdot \boldsymbol{\sigma}_c \nabla \phi_c = 0 \text{ on } \Omega_C \backslash \Omega_P, \tag{1.7}$$

$$\vec{n}_H \cdot \boldsymbol{\sigma}_c \nabla \phi_c = \vec{n}_H \cdot \boldsymbol{\sigma}_e \nabla \phi_e = J_H \text{ and } \phi_c = \phi_e \text{ on } \Gamma_H, \tag{1.8}$$

$$\vec{n}_C \cdot \boldsymbol{\sigma}_c \nabla \phi_c = 0 \text{ on } \Gamma_C, \tag{1.9}$$

$$\phi_c = \phi_p \text{ on } \Omega_P. \tag{1.10}$$

As shown in Figure 1.5, the torso is composed of several kinds of organs that have different electric conductivities. Table 1.2 lists the conductivities of the organs present in our simulation. As depicted by the broken line in Figure 1.4, we observed substantially different computational results for the body surface potential when we assumed

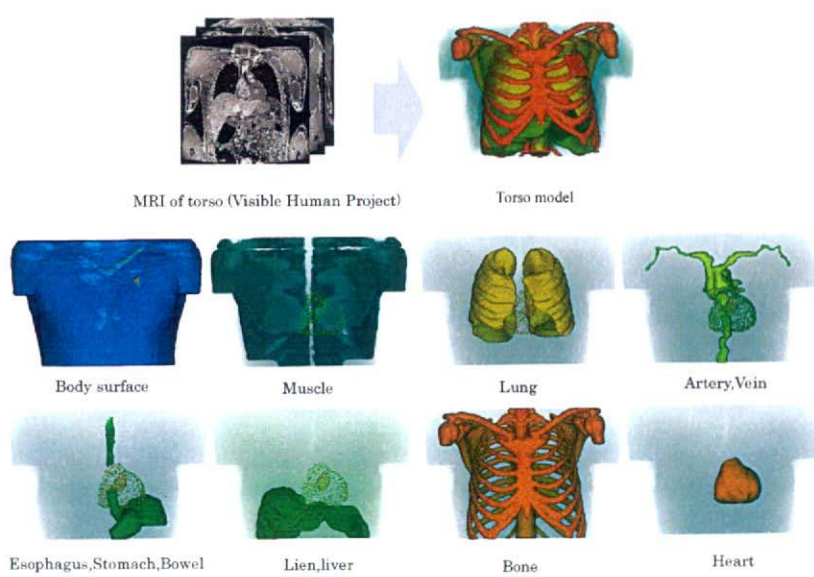

FIG. 1.5. *Organs in the torso.*

TABLE 1.2
Conductivities [mS/cm] of the organs outside the heart muscle.

Blood	7.8	Capsula cordis	15.0
Muscle	2.56	Lung	0.83
Artery, vein	6.8	Esophagus	2.0
Stomach, bowel	2.0	Lien, liver	1.67
Bone	0.06	Others	0.5

a totally homogeneous conductivity (3 mS/cm) on the torso. This indicates the importance of modeling the torso conductance accurately.

In this paper, we present a technique for a parallel solution that handles the bidomain problem with the torso model in a robust and efficient way. In particular, we focus on a technique to overcome the difficulty of very high spatial resolution by using a sophisticated multigrid algorithm and parallel computation techniques. The multigrid algorithm is constructed for a conservative finite element discretization of the given potential problem on a composite mesh consisting of a fine local voxel mesh around the heart and a coarse global voxel mesh covering the torso. We also briefly present strategies to resolve the difficulty of time resolution. On one hand, more sophisticated adaptive refinement techniques have been proposed in earlier studies [4, 14, 24] where the refinement is varied over time depending on the ongoing electric activity. However, on the other hand, this study is significantly more complex since the method is shown to be applicable to a problem of practical interest, whereas the earlier study has merely shown the feasibility of the method on a simple two-dimensional grid. Some previous works [17, 26] also adopt a multigrid method for the bidomain problem. However, neither the composite mesh problem nor the Purkinje network is dealt with in these studies. The differences between this research and the earlier studies mentioned above are summarized below.

1. A stability analysis of a typical explicit time integration scheme of the bidomain equation [24, 26] is given.
2. A conservative finite element discretization of the potential problem on the composite mesh is proposed by applying the Lagrange multiplier technique for the constraints at the interface of the local and global meshes.
3. A multigrid solution method for the discretization on the composite mesh is derived naturally by the Lagrange multiplier at the interface.
4. The conservation property of the electric currents passing through the electrodes is investigated. This is important when considering the interaction with an external electrical device, such as an ICD.
5. An efficient way of dealing with the Purkinje fiber network in the multigrid method is proposed.

In our simulator, the Purkinje fibers are modeled as one-dimensional multiway branching lines connected to the voxel nodes at these end-points, as has been reported in the literature [22]. Bidomain equations similar to (1.1), (1.2), and (1.5) are then discretized by the one-dimensional finite elements constructed on the network. In this situation, the voxel mesh can be coarsened in a standard way by exploiting its regular structure, whereas the Purkinje network is irregular. Thus, combining the Purkinje network with the multigrid algorithm is not straightforward. We also present a practical parallel implementation method on a distributed memory machine. Good performance of the implemented algorithm is demonstrated through numerical experiments with a realistic human heart model that includes the torso. Note that unstructured grids are preferred for the defibrillation studies with an ICD, since smooth boundaries are required to avoid artificial currents at the strong shock. Efficiency of the algebraic multigrid method in such cases is confirmed in the literature [15] for rabbit ventricles. In our case, we adopted the voxel mesh approach due to the simplicity of modeling and data handling, ease of parallelization, and faster computation speed by avoiding indirect memory addressing.

2. Finite element discretization. In this section, we introduce the temporal and spatial discretization of the bidomain equation. The weak forms of (1.1)–(1.4) on

Ω_H are given by

$$\int_{\Omega_H} \nabla w_{\rm i} \cdot \boldsymbol{\sigma}_{\rm i} \nabla \phi_{\rm i} d\Omega = -\int_{\Omega_H} w_{\rm i} \beta I_{\rm m} d\Omega, \tag{2.1}$$

$$\int_{\Omega_H} \nabla w_{\rm e} \cdot \boldsymbol{\sigma}_{\rm e} \nabla \phi_{\rm e} d\Omega = \int_{\Omega_H} w_{\rm e} \beta I_{\rm m} d\Omega + \int_{\Gamma_H} w_{\rm e} J_H d\Gamma. \tag{2.2}$$

Furthermore, the weak form of (1.7)–(1.9) on Ω_C is given by

$$\int_{\Omega_C \backslash \Omega_P} \nabla w_{\rm c} \cdot \boldsymbol{\sigma}_{\rm c} \nabla \phi_{\rm c} d\Omega = -\int_{\Gamma_H} w_{\rm c} J_H d\Gamma, \ w_{\rm c} = 0 \text{ on } \Gamma_P. \tag{2.3}$$

Here, $w_{\rm i}, w_{\rm e}$, and $w_{\rm c}$ are arbitrary test functions. With the boundary conditions on Γ_H given in (1.8), we can superpose the two extracellular equations on Ω_H and Ω_C, and replace (2.2) and (2.3) by

$$\int_{\Omega} \nabla w_{\rm e} \cdot \boldsymbol{\sigma}_{\rm e} \nabla \phi_{\rm e} d\Omega = \int_{\Omega_H} w_{\rm e} \beta I_{\rm m} d\Omega, \tag{2.4}$$

$$\phi_{\rm e} = \phi_{\rm p}, \ w_{\rm e} = 0 \text{ on } \Gamma_P. \tag{2.5}$$

Here, $\Omega = \Omega_H \cup \Omega_C \backslash \Omega_P$ and Γ_P is the boundary of Ω_P. The extracellular potentials and the conductivity tensors are combined on the whole domain Ω as

$$\phi_{\rm e} = \begin{cases} \phi_{\rm e} & \text{on } \Omega_H, \\ \phi_{\rm c} & \text{on } \Omega_C, \end{cases} \qquad \boldsymbol{\sigma}_{\rm e} = \begin{cases} \boldsymbol{\sigma}_{\rm e} & \text{on } \Omega_H, \\ \boldsymbol{\sigma}_{\rm c} & \text{on } \Omega_C. \end{cases} \tag{2.6}$$

The matrix representation for a finite element discretization of the intracellular equation on Ω_H in (2.1) and the extracellular equation on Ω in (2.4) is given by

$$\boldsymbol{K}_{\rm i} \boldsymbol{\phi}_{\rm i} = -\beta \boldsymbol{I}_{\rm m}, \tag{2.7}$$

$$\boldsymbol{K}_{\rm e} \boldsymbol{\phi}_{\rm e} = \boldsymbol{R}_H{}^T \beta \boldsymbol{I}_{\rm m} - \boldsymbol{K}_{\rm p} \boldsymbol{\phi}_{\rm p}. \tag{2.8}$$

Here, we assume that the nodes on the electrodes are deleted in the vector representation $\boldsymbol{\phi}_{\rm e}$, and that $\boldsymbol{R}_H$ represents a restriction operator from the whole domain Ω to the subdomain Ω_H on the heart muscle. Since $\boldsymbol{R}_H$ is a simple injection on Ω_H in our case, we will omit $\boldsymbol{R}_H$ and its transpose $\boldsymbol{R}_H^T$ in the equations hereafter. For example, the matrices $\boldsymbol{R}_H^T \boldsymbol{K}_{\rm i}$ and $\boldsymbol{R}_H^T \boldsymbol{K}_{\rm i} \boldsymbol{R}_H$ will simply be represented by $\boldsymbol{K}_{\rm i}$.

2.1. Explicit time integration scheme. In order to establish a stable time integration scheme, (2.7) and (2.8) are rewritten as

$$\boldsymbol{K}_{\rm i} \boldsymbol{V}_{\rm m} + \beta \boldsymbol{I}_{\rm m} + \boldsymbol{K}_{\rm i} \boldsymbol{\phi}_{\rm e} = \boldsymbol{0}, \tag{2.9}$$

$$\boldsymbol{K}_{\rm i} \boldsymbol{V}_{\rm m} + (\boldsymbol{K}_{\rm i} + \boldsymbol{K}_{\rm e}) \boldsymbol{\phi}_{\rm e} = -\boldsymbol{K}_{\rm p} \boldsymbol{\phi}_{\rm p}. \tag{2.10}$$

Equation (2.10) is obtained by adding (2.7) and (2.8) and the relation between the potentials, $\boldsymbol{V}_{\rm m} = \boldsymbol{\phi}_{\rm i} - \boldsymbol{\phi}_{\rm e}$ on Ω_H. Note that the intracellular potential disappears in this representation, and the second equation (2.10) does not contain the transmembrane current $I_{\rm m}$. The system of (2.9) and (2.10) can be integrated stably along the temporal axis in either an explicit or a semi-implicit manner. In our case, we adopt the following explicit method to reduce the computational costs [24]. The matrix representation of the explicit scheme is given by

$$\begin{aligned} \begin{bmatrix} \frac{\beta C_{\rm m}}{\Delta t} \boldsymbol{M}_H & \boldsymbol{0} \\ \boldsymbol{K}_{\rm i} & \boldsymbol{K}_{\rm i} + \boldsymbol{K}_{\rm e} \end{bmatrix} \begin{bmatrix} \boldsymbol{V}_{\rm m}^{t+\Delta t} \\ \boldsymbol{\phi}_{\rm e}^{t+\Delta t} \end{bmatrix} = & \begin{bmatrix} \frac{\beta C_{\rm m}}{\Delta t} \boldsymbol{M}_H - \boldsymbol{K}_{\rm i} & -\boldsymbol{K}_{\rm i} \\ \boldsymbol{0} & \boldsymbol{0} \end{bmatrix} \begin{bmatrix} \boldsymbol{V}_{\rm m}^{t} \\ \boldsymbol{\phi}_{\rm e}^{t} \end{bmatrix} \\ & - \begin{bmatrix} \beta \boldsymbol{M}_H & \boldsymbol{0} \\ \boldsymbol{0} & \boldsymbol{K}_{\rm p} \end{bmatrix} \begin{bmatrix} \boldsymbol{I}_{\rm ion}(\boldsymbol{V}_{\rm m}^t, \boldsymbol{S}^t) \\ \boldsymbol{\phi}_{\rm p}^{t+\Delta t} \end{bmatrix}, \end{aligned} \tag{2.11}$$

where $\boldsymbol{M}_H$ is the lumped matrix on Ω_H and $\phi_{\mathrm{p}}^{t+\Delta t}$ is a prescribed potential on the electrodes. In the semi-implicit scheme as adopted in the literature [17], the entire PDE system (except for the ODEs to compute $\boldsymbol{S}$) is solved simultaneously. This scheme requires almost quadruple the computational costs for the matrix vector multiplication and the relaxation phase. On the other hand, the time step size Δt is usually determined in accordance with the ODE system to compute the state vector $\boldsymbol{S}$ as described later. Thus, we have adopted the explicit scheme in our simulator. If we ignore the time dependence of I_{ion} in (2.11), the stability of the explicit scheme depends on the spectral radius of the matrix:

$$\mathcal{M} = \begin{bmatrix} \boldsymbol{D}_{\mathrm{m}} & 0 \\ \boldsymbol{K}_{\mathrm{i}} & \boldsymbol{K}_{\mathrm{i}} + \boldsymbol{K}_{\mathrm{e}} \end{bmatrix}^{-1} \begin{bmatrix} \boldsymbol{D}_{\mathrm{m}} - \boldsymbol{K}_{\mathrm{i}} & -\boldsymbol{K}_{\mathrm{i}} \\ 0 & 0 \end{bmatrix}, \tag{2.12}$$

with

$$\boldsymbol{D}_{\mathrm{m}} = \frac{\beta C_{\mathrm{m}}}{\Delta t} \boldsymbol{M}_H. \tag{2.13}$$

The spectral radius of $\mathcal{M}$ is bounded above as described by the following.

THEOREM 2.1. *Assume the spectral radius of* $\boldsymbol{D}_{\mathrm{m}}^{-1}\boldsymbol{K}_{\mathrm{i}}$ *is less than one.*

$$\rho(\boldsymbol{D}_{\mathrm{m}}^{-1}\boldsymbol{K}_{\mathrm{i}}) < 1. \tag{2.14}$$

Then the spectral radius of $\mathcal{M}$ *in* (2.12) *is bounded as*

$$\rho(\mathcal{M}) \leq 1 - \lambda_{\min}(\boldsymbol{D}_{\mathrm{m}}^{-1}\boldsymbol{K}_{\mathrm{i}})(1 - \lambda_{\max}((\boldsymbol{K}_{\mathrm{i}} + \boldsymbol{K}_{\mathrm{e}})^{-1}\boldsymbol{K}_{\mathrm{i}})). \tag{2.15}$$

Here, $\lambda_{\min}$ *and* $\lambda_{\max}$ *represent, respectively, the minimum and maximum eigenvalues of the matrices in brackets.*

A proof of the theorem is given in Appendix A. From the theorem, we see that the scheme is stable if condition (2.14) is satisfied and the time dependence of I_{ion} is ignored. In the actual simulation, however, a fairly small time step, far smaller than the above limitation, is required to compute the ion currents $I_{\mathrm{ion}}(V_{\mathrm{m}}, \boldsymbol{S})$ in (1.5) (see [23]). Thus, we can adopt an "inner-outer" time integration strategy where the intracellular (2.9) is integrated with a small time step in the inner iterations while fixing the extracellular potential ϕ_{e}, and the extracellular potential ϕ_{e} is updated only in the outer iteration with a large time step. This strategy has been adopted extensively by many studies [24]. The algorithm is presented in Figure 2.1. Here, the superscripts denote the time indices for the variables, where T is the time index for solving the extracellular potential problem and t is the time index for integrating the membrane potential. At each inner iteration, the ODE to compute the state vector $\boldsymbol{S}$ is solved by the explicit Euler scheme. The time step δt (typically $10\sim100\mu$s) is flexibly varied in time and space depending on the ongoing electric activity as described in the literature [24]. At each outer iteration, a solution to the potential problem on Ω is required. The time steps ΔT and Δt are adjusted flexibly depending on the simulation conditions and the desired accuracy of the solution. For example, in Figure 2.2, the two curves represent the second-lead ECG results as explained in section 1 for time steps $\Delta T = 0.2$ ms and $\Delta T = 1$ ms, respectively. Though both curves show a similar tendency and magnitude of fluctuation, substantial phase lag is observed.

Even when adopting a large time step for ΔT in the above inner-outer time integration scheme, the speedup of the solution to the extracellular potential problem is the key issue for the overall performance. Henceforth, we will focus on an efficient discretization of and solution method for the potential problem.

The inner-outer time integration scheme.
Given $\boldsymbol{V}_{\mathrm{m}}^{t_0}$
Solve $(\boldsymbol{K}_{\mathrm{i}} + \boldsymbol{K}_{\mathrm{e}})\boldsymbol{\phi}_{\mathrm{e}}^{t_0} = -\boldsymbol{K}_{\mathrm{p}}\boldsymbol{\phi}_{\mathrm{p}}^{t_0} - \boldsymbol{K}_{\mathrm{i}}\boldsymbol{V}_{\mathrm{m}}^{t_0}$
for $k = 1, \ldots, k_{\mathrm{end}}$
  $T = t_0 + (k-1)\Delta T$
  for $i = 1, \ldots, \Delta T/\Delta t$
    $t = (i-1)\Delta t + T$
    $\boldsymbol{V}_{\mathrm{m}}^{t+\Delta t} = \boldsymbol{V}_{\mathrm{m}}^{t} - \frac{\Delta t}{\beta C_{\mathrm{m}}}\boldsymbol{M}_H^{-1}\boldsymbol{K}_{\mathrm{i}}\boldsymbol{V}_{\mathrm{m}}^{t} - \boldsymbol{K}_{\mathrm{i}}\boldsymbol{\phi}_{\mathrm{e}}^{T} - \frac{\Delta t}{\beta C_{\mathrm{m}}}\boldsymbol{I}_{\mathrm{ion}}(\boldsymbol{V}_{\mathrm{m}}^{t}, \boldsymbol{S}^{t})$
  next i
  Solve $(\boldsymbol{K}_{\mathrm{i}} + \boldsymbol{K}_{\mathrm{e}})\boldsymbol{\phi}_{\mathrm{e}}^{T+\Delta T} = -\boldsymbol{K}_{\mathrm{p}}\boldsymbol{\phi}_{\mathrm{p}}^{T+\Delta T} - \boldsymbol{K}_{\mathrm{i}}\boldsymbol{V}_{\mathrm{m}}^{T+\Delta T}$
next k

FIG. 2.1. *The inner-outer time integration scheme.*

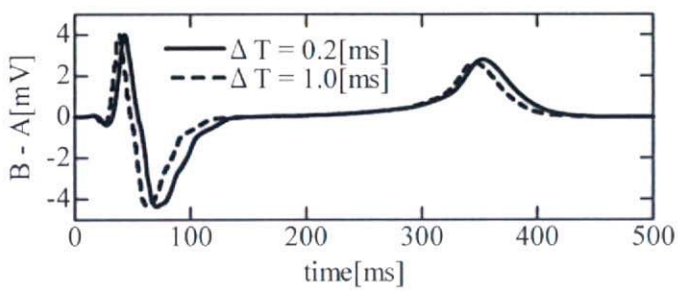

FIG. 2.2. *The second-lead ECG for two different time steps.*

2.2. Spatial discretization of a composite voxel mesh. Hereafter, $\boldsymbol{\sigma}$ denotes $\boldsymbol{\sigma}_{\mathrm{e}} + \boldsymbol{\sigma}_{\mathrm{i}}$, and ϕ denotes ϕ_e for notational convenience. The weak form corresponding to (2.10) is given by

$$\int_{\Omega} \nabla w \cdot \boldsymbol{\sigma} \nabla \phi d\Omega = -\int_{\Omega_H} \nabla w \cdot \boldsymbol{\sigma}_{\mathrm{i}} \nabla V_{\mathrm{m}} d\Omega,$$
$$w = 0 \text{ and } \phi = \phi_{\mathrm{p}} \text{ on } \Gamma_P. \tag{2.16}$$

To discretize the above equation, we adopt a uniform three-dimensional voxel mesh because this allows the input data to be prepared easily and it facilitates the implementation of the multigrid solver and the parallelization of the code. For the intracellular equations (1.1) and (1.5) on the heart, a fine spatial resolution (0.15 mm $\sim$ 0.4 mm) is required to attain sufficient accuracy. On the other hand, such a fine resolution is unnecessary for the extracellular equation (2.4) outside the heart. The above fact naturally leads to the use of two meshes with different spatial resolutions. One is the finer mesh on the local rectangular parallelepiped domain around the heart. The other is the coarser mesh on the global rectangular parallelepiped domain covering the whole torso (see Figure 2.3). Henceforth, we refer to the former mesh as the local mesh and to the latter as the global mesh. We assume that the nodes in the global mesh on the local rectangular parallelepiped domain are given at the same positions as those in the local mesh, and the interval ratio of the global to local mesh is a power of two. Note that it is not necessarily just two as in the usual local refinement. For example, four or eight can also be handled in our framework.

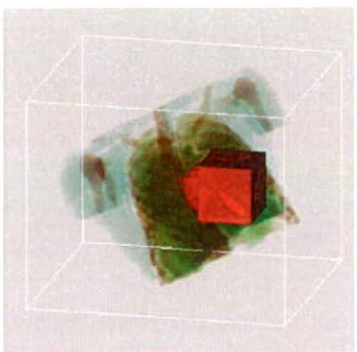

FIG. 2.3. *The fine local voxel mesh domain around the heart and the global coarse voxel mesh domain covering the torso.*

In order to discretize (2.16) on the composite mesh, we apply the Lagrange multiplier method for the constraints at the interface of the local and global meshes. Therefore, we start with a variational formulation of the problem. The energy functional for the formulation is given by

$$\mathcal{E}(\phi) = \int_\Omega \frac{1}{2}\nabla\phi\cdot\boldsymbol{\sigma}\nabla\phi d\Omega + \int_{\Omega_H} \nabla\phi\cdot\boldsymbol{\sigma}_{\mathrm{i}}\nabla V_{\mathrm{m}} d\Omega, \qquad \phi = \phi_{\mathrm{p}} \text{ on } \Gamma_P. \tag{2.17}$$

The extremum of the energy functional in (2.17) satisfies (2.16). Let Ω^L and Ω^G be the local and global meshes, respectively. In particular, Ω^L is a local refinement of Ω^G. In the following, Ω^L and Ω^G are identified either as the domains covered by the meshes or as the sets of nodes in them. Let E^L and E^G be the sets of finite elements contained in Ω^L and Ω^G, respectively. Let Ω^G_L and $\overline{\Omega^G_L}$ be the subsets of Ω^G on Ω^L and outside of Ω^L, respectively. Let E^G_L and $\overline{E^G_L}$ be the subsets of E^G which lie in Ω^G_L and $\overline{\Omega^G_L}$, respectively (see Figure 2.4). We represent an interpolated function ϕ^L for the nodal values $\boldsymbol{\phi}^L$ on the local mesh Ω^L by

$$\phi^L = \boldsymbol{N}^L\cdot\boldsymbol{\phi}^L = \sum_{i\in\Omega^L} N^L_i\phi^L_i. \tag{2.18}$$

Here, $\{N^L_i\}_{i\in\Omega^L}$ are the shape functions on Ω^L. We use similar notation, $\boldsymbol{N}^G, N^G_i, \phi^G$, etc., for the global mesh Ω^G.

Under the above definitions, we define an energy functional for a given nodal function $\boldsymbol{\phi} = \{\boldsymbol{\phi}^L, \boldsymbol{\phi}^G\}$ on the composite mesh by

$$\begin{aligned}\mathcal{E}(\phi) &= \int_{\Omega_L}\frac{1}{2}\nabla\phi^L\cdot\boldsymbol{\sigma}\nabla\phi^L d\Omega + \int_{\overline{\Omega^G_L}}\frac{1}{2}\nabla\phi^G\cdot\boldsymbol{\sigma}\nabla\phi^G d\Omega + \int_{\Omega_H}\nabla\phi^L\cdot\boldsymbol{\sigma}_{\mathrm{i}}\nabla V^L_{\mathrm{m}} d\Omega\\ &= \sum_{e^L\in E^L}\int_{e^L}\frac{1}{2}\nabla\boldsymbol{N}^L\boldsymbol{\phi}^L\cdot\boldsymbol{\sigma}\nabla\boldsymbol{N}^L\boldsymbol{\phi}^L d\Omega + \sum_{e^G\in\overline{E^G_L}}\int_{e^G}\frac{1}{2}\nabla\boldsymbol{N}^G\boldsymbol{\phi}^G\cdot\boldsymbol{\sigma}\nabla\boldsymbol{N}^G\boldsymbol{\phi}^G d\Omega\\ &\quad + \sum_{e^L\in E^L_H}\int_{e^L}\nabla\boldsymbol{N}^L\boldsymbol{\phi}^L\cdot\boldsymbol{\sigma}_{\mathrm{i}}\nabla\boldsymbol{N}^L\boldsymbol{V}^L_{\mathrm{m}} d\Omega.\end{aligned} \tag{2.19}$$

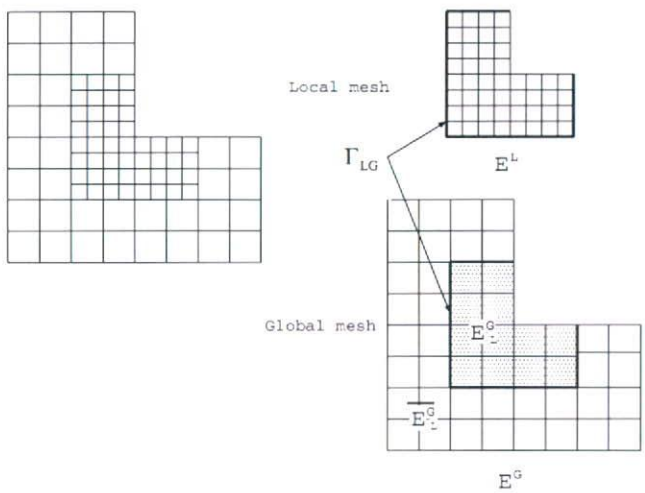

FIG. 2.4. *A composite mesh (left) and decomposition of the elements into the subsets for each level (right).*

Here, E_H^L are elements in E^L that lie in Ω_H. Note that we assume that Ω_H is composed of a subset of E^L. Now, we impose the following constraint conditions on the variational problem.

$$\phi^L = \boldsymbol{I}_G^L \phi^G \text{ on } \Gamma_{LG}. \tag{2.20}$$

Here, $\boldsymbol{I}_G^L$ is an interpolation operator from Ω^G to Ω^L and Γ_{LG} is the set of nodes situated at the interface boundaries of Ω^L with Ω^G. Note that Γ_{LG} is not necessarily identical to the boundary of Ω^L. As shown by the thick lines in the diagram on the right of Figure 2.4, the intersections of $\partial\Omega$ and $\partial\Omega_L$ are not contained in Γ_{LG}. The weights of the interpolation are determined by the shape functions $\boldsymbol{N}^G$ on Ω^G.

Let $\dot{\Omega}_L^G$ be the set of internal nodes in Ω_L^G where the nodes on Γ_{LG} are excluded. The components of ϕ^G on $\dot{\Omega}_L^G$ do not affect the functional in (2.19). However, these components are set identical to ϕ^L by an injection of the solution as described in section 3.1.

The following equation is obtained by applying the Lagrange multiplier method to the variational problem (2.19).

$$\begin{aligned}\int_{\Omega^L} \nabla w^L \cdot \boldsymbol{\sigma} \nabla \phi^L d\Omega + \int_{\overline{\Omega_L^G}} \nabla w^G \cdot \boldsymbol{\sigma} \nabla \phi^G d\Omega + \int_{\Omega_H^L} \nabla w^L \cdot \boldsymbol{\sigma}_{\mathrm{i}} \nabla V_{\mathrm{m}}^L d\Omega \\ + \left(\boldsymbol{w}^L - \boldsymbol{I}_G^L \boldsymbol{w}^G\right)_{\Gamma_{LG}} \cdot \boldsymbol{\lambda} + \boldsymbol{w}_\lambda \cdot \left(\phi^L - \boldsymbol{I}_G^L \phi^G\right)_{\Gamma_{LG}} = 0.\end{aligned} \tag{2.21}$$

Here, w^L and w^G are arbitrary test functions equal to zero on Γ_P. The brackets $(\,)_{\Gamma_{LG}}$ denote the restriction of a vector to the nodes on Γ_{LG}, $\boldsymbol{\lambda}$ is the Lagrange multiplier defined at the nodes on Γ_{LG}, and $\boldsymbol{w}_\lambda$ is a test vector associated with the Lagrange multiplier. Equation (2.21) can be rewritten in matrix form as follows:

$$\begin{aligned}\boldsymbol{w}^L \cdot \left(\boldsymbol{K}^L \phi^L + \boldsymbol{K}_{\mathrm{i}}^L \boldsymbol{V}_{\mathrm{m}}^L\right) + \boldsymbol{w}^G \cdot \overline{\boldsymbol{K}_L^G} \phi^G + \left(\boldsymbol{w}^L - \boldsymbol{I}_G^L \boldsymbol{w}^G\right)_{\Gamma_{LG}} \cdot \boldsymbol{\lambda} \\ + \boldsymbol{w}_\lambda \cdot \left(\phi^L - \boldsymbol{I}_G^L \phi^G\right)_{\Gamma_{LG}} = 0.\end{aligned} \tag{2.22}$$

Here, the matrices $\boldsymbol{K}^L$, $\boldsymbol{K}_{\mathrm{i}}^L$, and $\overline{\boldsymbol{K}_L^G}$ are obtained by superposing element matrices as

$$\boldsymbol{K}^L = \sum_{e^L \in E^L} \boldsymbol{K}^L(e^L), \tag{2.23}$$

$$\boldsymbol{K}_{\mathrm{i}}^L = \sum_{e^L \in E^L} \boldsymbol{K}_{\mathrm{i}}^L(e^L), \tag{2.24}$$

$$\overline{\boldsymbol{K}_L^G} = \sum_{e^G \in \overline{E_L^G}} \boldsymbol{K}^G(e^G), \tag{2.25}$$

where the element matrices are given by

$$\boldsymbol{K}^L(e^L)_{ij} = \int_{e^L} \nabla N_i^L \cdot \boldsymbol{\sigma} \nabla N_j^L d\Omega, \tag{2.26}$$

$$\boldsymbol{K}_{\mathrm{i}}^L(e^L)_{ij} = \int_{e^L} \nabla N_i^L \cdot \boldsymbol{\sigma}_{\mathrm{i}} \nabla N_j^L d\Omega, \tag{2.27}$$

$$\boldsymbol{K}^G(e^G)_{ij} = \int_{e^G} \nabla N_i^G \cdot \boldsymbol{\sigma} \nabla N_j^G d\Omega \tag{2.28}$$

for nodes i and j of elements e^L and e^G. From (2.22), we finally obtain

$$\boldsymbol{K}^L \boldsymbol{\phi}^L + \boldsymbol{K}_{\mathrm{i}}^L \boldsymbol{V}_{\mathrm{m}}^L + \boldsymbol{\lambda} = \boldsymbol{0} \text{ on } \Omega^L \backslash \Gamma_P, \tag{2.29}$$

$$\overline{\boldsymbol{K}_L^G} \boldsymbol{\phi}^G - \boldsymbol{I}_G^{L\,T} \boldsymbol{\lambda} = \boldsymbol{0} \text{ on } \overline{\Omega_L^G} \backslash \Gamma_P, \tag{2.30}$$

$$\boldsymbol{\phi}^L = \boldsymbol{\phi}_{\mathrm{p}} \text{ and } \boldsymbol{\phi}^G = \boldsymbol{\phi}_{\mathrm{p}} \text{ on } \Gamma_P$$

with the constraint condition in (2.20). In section 3.1, we derive a local-global multigrid solution algorithm for (2.29) and (2.30). From (2.29), the nodal values of the Lagrange multiplier at Γ_{LG} can be interpreted as the electric currents from the local mesh. In other words, the electric currents passing through the element surface from the local mesh elements are integrated on the local nodes at the interface. In (2.30), these nodal values of the currents from the local mesh are distributed by $\boldsymbol{I}_G^{L\,T}$ to the global mesh nodes at Γ_{LG}, and they are balanced with the currents from the global mesh elements in $\overline{E_L^G}$. In this way, the current balance is ensured at the interface. In the next section, we will see that this results in the conservation of the electric currents passing through the electrodes.

2.3. Conservation properties of the electric currents passing through the electrodes. For simplicity, at first we assume that the boundaries Γ_P of the electrodes do not intersect with the interface boundary Γ_{LG}. Later, this condition is relaxed to some extent. The above assumption implies that the nodes on Γ_P are exclusively divided into local and global sections.

$$\Gamma_P = \Gamma_P^L \cup \Gamma_P^G. \tag{2.31}$$

We define the nodal residual components at nodes $i \in \Gamma_P^L$ and $j \in \Gamma_P^G$ by

$$r_i^L = -\int_{\Omega^L} \nabla N_i^L \cdot (\boldsymbol{\sigma} \nabla \phi^L + \boldsymbol{\sigma}_{\mathrm{i}} \nabla V_{\mathrm{m}}^L) d\Omega = -(\boldsymbol{K}^L \boldsymbol{\phi}^L + \boldsymbol{K}_{\mathrm{i}}^L \boldsymbol{V}_{\mathrm{m}}^L)_i, \ i \in \Gamma_P^L, \tag{2.32}$$

$$r_j^G = -\int_{\overline{\Omega_L^G}} \nabla N_j^G \cdot \boldsymbol{\sigma} \nabla \phi^G d\Omega = -(\overline{\boldsymbol{K}_L^G} \boldsymbol{\phi}^G)_j, \ j \in \Gamma_P^G. \tag{2.33}$$

The conservation law through the entire domain Ω in the finite element context is stated below.

THEOREM 2.2. *Assume that* $\{\phi^L, \phi^G\}$ *is the finite element solution to* (2.21). *Then*

$$\sum_{i\in\Gamma_P^L} r_i^L + \sum_{j\in\Gamma_P^G} r_j^G = 0. \tag{2.34}$$

Proof. For the local and global meshes, let us define the following test functions.

$$w^L = 1 - \sum_{i\in\Gamma_P^L} N_i^L, \tag{2.35}$$

$$w^G = 1 - \sum_{j\in\Gamma_P^G} N_j^G. \tag{2.36}$$

From the assumption on Γ_P, $\boldsymbol{w}^L \equiv 1$ on Γ_{LG} and $\boldsymbol{w}^G \equiv 1$ on Γ_{LG}. Thus, from the natural requirement on the interpolation $\boldsymbol{I}_G^L$ we see that

$$\boldsymbol{I}_G^L \boldsymbol{w}^G \equiv \boldsymbol{w}^L = 1 \text{ on } \Gamma_{LG}. \tag{2.37}$$

By substituting (2.35), (2.36), and (2.37) into (2.21), we obtain

$$\int_{\Omega^L} \nabla(1 - \sum_{i\in\Gamma_P^L} N_i^L)\cdot\boldsymbol{\sigma}\nabla\phi^L d\Omega + \int_{\Omega_L^G} \nabla(1 - \sum_{j\in\Gamma_P^G} N_j^G)\cdot\boldsymbol{\sigma}\nabla\phi^G d\Omega + \int_{\Omega_H^L} \nabla(1 - \sum_{i\in\Gamma_P^L} N_i^L)\cdot\boldsymbol{\sigma}_{\mathrm{i}}\nabla V_{\mathrm{m}}^L d\Omega = 0.$$

By expanding the above equation, we obtain (2.34). ∎

Physically, the residual at the electrode boundaries Γ_P can be interpreted as the current entering the torso through the surface of the electrodes. Here we assume that the weak solution ϕ to (2.16) is also the strong solution around Γ_p under a certain regularity of $\boldsymbol{\sigma}_{\mathrm{e}}$. That is, if the strong form equation

$$-\nabla\cdot\boldsymbol{\sigma}_{\mathrm{e}}\nabla\phi = 0 \text{ around } \Gamma_P \tag{2.38}$$

holds, we obtain from the Gauss divergence theorem

$$-\int_{\Omega^L} \nabla N_i^L\cdot\boldsymbol{\sigma}_{\mathrm{e}}\nabla\phi d\Omega = -\int_{\Gamma_P^L} N_i^L\vec{n}\cdot\boldsymbol{\sigma}_{\mathrm{e}}\nabla\phi d\Gamma,\ i\in\Gamma_P^L, \tag{2.39}$$

$$-\int_{\Omega^G} \nabla N_j^G\cdot\boldsymbol{\sigma}_{\mathrm{e}}\nabla\phi d\Omega = -\int_{\Gamma_P^G} N_j^G\vec{n}\cdot\boldsymbol{\sigma}_{\mathrm{e}}\nabla\phi d\Gamma,\ j\in\Gamma_P^G. \tag{2.40}$$

Here, $\vec{n}$ is the normal outward unit vector at Γ_P. Note that we assume that the electrode boundaries Γ_P are not attached to the heart muscle Ω_H. Thus, V_{m} and $\boldsymbol{\sigma}_{\mathrm{i}}$ do not appear in the equations. If we replace the analytical solution on the left-hand sides of (2.39) and (2.40) by the discrete finite element approximations, they are, in fact, the residual components. Thus, the residual components $r_i^L, i\in\Gamma_P^L$, and $r_j^G, j\in\Gamma_P^G$, are the approximations of the fluxes on the right-hand sides of (2.39) and (2.40), respectively. If the interaction with the electric circuit connected to the

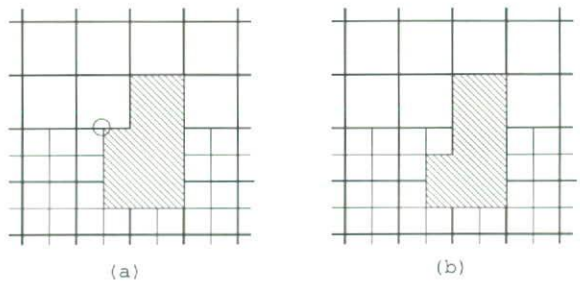

FIG. 2.5. *An undesired example for conservation* (a) *and the correction making this example conservative* (b). *In* (a), *a hanging node (marked with a circle) is located at the corner of the electrode.*

electrodes is taken into account, the summations of the residual components at the electrode surfaces can be identified with the currents from the electrodes.

So far we have assumed that the electrode surface Γ_P does not intersect the interface boundary Γ_{LG}. However, this restriction is not essential for the conservation, which is ensured as long as the boundaries Γ_{LG} follow the edges of the coarser elements at any interface. Figure 2.5 depicts an undesired example for conservation (a) and the correction making this example conservative (b). Note that a hanging node (marked with a circle) is located at the corner of the electrode in the undesired example. In general, we modify the definition of the test function w^L in (2.35) to match w^G in (2.36) at the interface.

$$w^L = 1 - \sum_{i \in \Gamma_P \setminus \Gamma_{LG}} N_i^L - \sum_{j \in \Gamma_P \cap \Gamma_{LG}} \boldsymbol{N}^L \left(\boldsymbol{I}_G^L \boldsymbol{\delta}_j^G \right)_{\Gamma_{LG}}. \tag{2.41}$$

Here, $\boldsymbol{\delta}_j^G$ is the vector on $\overline{\Omega_L^G}$ set to 1 at j and zero at the other nodes. From the above definition, we see that $\boldsymbol{I}_G^L \boldsymbol{w}^G \equiv \boldsymbol{w}^L$ holds at Γ_{LG}. By substituting this test function into (2.21), we once again obtain (2.34) with the following definition of the residual at the interface.

$$r_j = -(\overline{\boldsymbol{K}_L^G} \boldsymbol{\phi}^G)_j - \left(\boldsymbol{I}_G^{L\,T} (\boldsymbol{K}^L \boldsymbol{\phi}^L + \boldsymbol{K}_{\mathrm{i}}^L \boldsymbol{V}_{\mathrm{m}}^L) \right)_j, \quad j \in \Gamma_{LG} \cap \Gamma_P. \tag{2.42}$$

Thus, in computing the residual component at the interface, the contributions from the residual components on the neighboring fine mesh hanging nodes must be taken into account.

3. The local-global multigrid algorithm on a composite mesh.

3.1. Derivation of the algorithm. Let us define the matrices $\boldsymbol{K}_L^G$ and $\boldsymbol{K}^G$ on the global mesh by

$$\boldsymbol{K}_L^G = \sum_{e^G \in E_L^G} \boldsymbol{K}^G(e^G), \tag{3.1}$$

$$\boldsymbol{K}^G = \sum_{e^G \in E^G} \boldsymbol{K}^G(e^G). \tag{3.2}$$

From the above definitions and (2.25), $\boldsymbol{K}^G$ is obtained by superposing $\boldsymbol{K}_L^G$ and $\overline{\boldsymbol{K}_L^G}$. Thus,

$$\boldsymbol{K}^G = \boldsymbol{K}_L^G + \overline{\boldsymbol{K}_L^G}. \tag{3.3}$$

The local-global multigrid algorithm.
(0) Start
- $\boldsymbol{g}^L := -\boldsymbol{K}_{\mathrm{i}}^L \boldsymbol{V}_{\mathrm{m}}^L$
- Prepare an initial guess $\{\boldsymbol{\phi}^L, \boldsymbol{\phi}^G\}$ such that $\boldsymbol{\phi}^L = \boldsymbol{I}_G^L \boldsymbol{\phi}^G$ on Γ_{LG}

(1) Global mesh correction
- Compute the residual on the local mesh $\boldsymbol{r}^L := \mathbf{g}^L - \boldsymbol{K}^L \boldsymbol{\phi}^L$ on $\Omega^L \backslash \Gamma_P$
- Inject the local mesh solution $\boldsymbol{\phi}^G := \hat{\boldsymbol{I}}_L^G \boldsymbol{\phi}^L$ on Ω_{i}^G
- Store $\boldsymbol{\phi}^G$ in another vector $\hat{\boldsymbol{\phi}}^G := \boldsymbol{\phi}^G$
- Compute the right-hand side $\mathbf{g}^G := \boldsymbol{K}_L^G \hat{\boldsymbol{\phi}}^G + \boldsymbol{I}_G^{L\,T} \boldsymbol{r}^L$
- Compute an approximation for $\boldsymbol{K}^G \boldsymbol{\phi}^G = \mathbf{g}^G$ with the fixed boundary values on Γ_P
- Correction with the interpolation $\boldsymbol{\phi}^L := \boldsymbol{\phi}^L + \boldsymbol{I}_G^L (\boldsymbol{\phi}^G - \hat{\boldsymbol{\phi}}^G)$ on Ω^L

(2) Smoothing on the local mesh
- Relax the interior components of $\boldsymbol{\phi}^L$ for $\boldsymbol{K}^L \boldsymbol{\phi}^L = \mathbf{g}^L$ with the fixed boundary values on $\Gamma_{LG} \cup \Gamma_P$

FIG. 3.1. *The local-global multigrid algorithm.*

Based on the idea proposed by Brandt [2], we add $\boldsymbol{K}_L^G \boldsymbol{\phi}^G$ to both sides of (2.30). Then we obtain the following equations equivalent to (2.29) and (2.30).

$$\boldsymbol{K}^L \boldsymbol{\phi}^L = -\boldsymbol{K}_{\mathrm{i}}^L \boldsymbol{V}_{\mathrm{m}}^L \text{ on } \Omega^L \backslash (\Gamma_{LG} \cup \Gamma_P), \tag{3.4}$$

$$\boldsymbol{\lambda} = -\boldsymbol{K}^L \boldsymbol{\phi}^L - \boldsymbol{K}_{\mathrm{i}}^L \boldsymbol{V}_{\mathrm{m}}^L \text{ on } \Gamma_{LG}, \tag{3.5}$$

$$\boldsymbol{K}^G \boldsymbol{\phi}^G = \boldsymbol{I}_G^{L\,T} \boldsymbol{\lambda} + \boldsymbol{K}_L^G \boldsymbol{\phi}^G \text{ on } \Omega^G \backslash \Gamma_P. \tag{3.6}$$

If we define the residual vector $\boldsymbol{r}^L$ on the local mesh from (3.4), not only on $\Omega^L \backslash (\Gamma_{LG} \cup \Gamma_P)$, but also on Γ_{LG} by

$$\boldsymbol{r}^L = -\boldsymbol{K}_{\mathrm{i}}^L \boldsymbol{V}_{\mathrm{m}}^L - \boldsymbol{K}^L \boldsymbol{\phi}^L \text{ on } \Omega^L \backslash \Gamma_P, \tag{3.7}$$

we see that it is identical to the Lagrange multiplier on Γ_{LG} from (3.5).

$$\boldsymbol{\lambda} = \boldsymbol{r}^L \text{ on } \Gamma_{LG}. \tag{3.8}$$

The above consideration naturally leads to the local-global solution process, shown in Figure 3.1, where (1) and (2) are iterated. Here, the injection $\hat{\boldsymbol{I}}_L^G$ is performed by injecting the local mesh nodal values into the global mesh nodes on Ω_L^G. Note that the correction with the interpolation is also performed on the interface Γ_{LG} in the global mesh correction phase. Thus, together with the assumption on the initial guess, the constraint condition in (2.20) is always satisfied. As for the relaxation on the local and global meshes, a multigrid V-cycle can be applied. In particular, for the local mesh relaxation, one V-cycle is sufficient to smooth the error with respect to the global mesh resolution, where the coarsest mesh of the V-cycle on the local mesh has the same spatial resolution as the global mesh in our implementation, as depicted in Figure 3.2.

The local-global multigrid algorithm obtained above is similar to the multilevel adaptive technique (MLAT) proposed by Brandt [2]. However, MLAT was described for finite difference or finite volume discretizations [20] and derived from the full

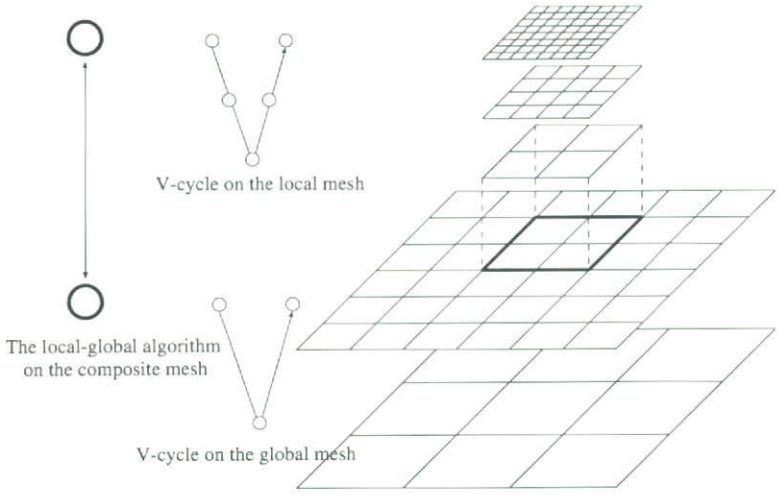

FIG. 3.2. *A sketch of the local-global multigrid algorithm. In each mesh, the multigrid V-cycle is applied as a smoother. In particular, the coarsest grid of the local mesh V-cycle has the same resolution as the finest global mesh.*

approximation scheme (FAS) [2, 20], originally proposed to solve a nonlinear problem with a multigrid. An interesting point here is that MLAT is naturally derived by extending the Lagrange multiplier in (3.6) at the local-global interface Γ_{LG} to the inside of the fine finite element mesh where it can be interpreted as the residual. Also note that in the standard implementation of MLAT [20], the residual at the fine grid boundary is not transferred to the coarse grid, whereas in the above algorithm the residual components at the local mesh interface boundaries certainly affect the right-hand side of the coarse mesh equation. As we have seen in section 2.3, this is an essential point to ensure the conservation property at the local-global interface. Other techniques to ensure the conservation have been introduced, for example, in [1, 12, 27] for finite volume discretizations. On the other hand, in common adaptive finite element approaches, a special refinement strategy is adopted at the fine-coarse interface so that hanging nodes are not present. In these approaches, conservation is automatically ensured. However, a method that allows hanging nodes provides easier mesh generation, in particular, for hexahedral elements.

3.2. Treatment of the Purkinje fiber network. In this section, we describe the special treatment of the Purkinje fibers in the local-global multigrid algorithm. As mentioned in section 1, the Purkinje network is modeled by one-dimensional elements, as is commonly done in the cardiovascular literature. In our simulator, only end-point nodes of the Purkinje network are connected to the voxel mesh nodes, as shown in Figure 3.3(a). Although a fairly fine spatial resolution is required for the Purkinje one-dimensional elements, we can eliminate most of the unknowns before solving the potential problem. This situation is illustrated in Figure 3.3. Nodes on the Purkinje network with only two edges connected can be eliminated without increasing the number of edges. Therefore, we do not apply any coarsening to the matrix on the reduced Purkinje nodes when constructing the matrix at the coarse level. In this case, although we have to invert the matrix completely on the reduced Purkinje nodes at the smoothing steps at each level of the multigrid cycle, this does not result in a